



Cite this: *Phys. Chem. Chem. Phys.*, 2022, 24, 13156

A computational study on the adsorption of arsenic pollutants on graphene-based single-atom iron adsorbents†

Kai Ma,^a Di Zheng,^a Weijie Yang,^a Chongchong Wu,^{*b} Shuai Dong,^a Zhengyang Gao^a and Xiaojun Zhao^c

Integrated gasification combined cycle (IGCC) is a promising clean technology for coal power generation; however, the high volatility and toxicity of arsenic pollutants (As₂, As₄, AsO and AsH₃) released from an IGCC coal plant cause serious damage to human health and the ecological environment. Therefore, highly efficient adsorbents for simultaneous treatment of multiple arsenic pollutants are urgently needed. In this work, the adsorption characteristics and competitive adsorption behaviors of As₂, As₄, AsO, and AsH₃ on four kinds of graphene-based single-atom iron adsorbents (Fe/GA) were systematically investigated through density functional theory (DFT) and *ab initio* molecular dynamics (AIMD) simulations. The results suggest that single-vacancy Fe/GA doped with three nitrogen atoms has the largest adsorption ability for As₂, As₄, AsO and AsH₃. The adsorption energies of As₂, AsO and As₄ on Fe/GA depend on both charge transfer and orbital hybridization, while the adsorption energy of AsH₃ is mainly decided by electronic transfer. The adsorption differences of As₂, As₄, AsO and AsH₃ on four Fe/GA adsorbents can be explained through the obvious linear relationship between the adsorption energy and Fermi softness. As₂, As₄, AsO and AsH₃ will compete for adsorption sites when they exist on the same adsorbent surface simultaneously, and the adsorption capacities of AsO and As₂ are relatively stronger. After the competitive adsorption between AsO and As₂, AsO occupies the adsorption site at 300–900 K. This theoretical work suggests that Fe/GA is a promising adsorbent for the simultaneous removal of multiple arsenic pollutants with high adsorption capacity and low cost.

Received 17th May 2021,
Accepted 18th April 2022

DOI: 10.1039/d1cp02170b

rsc.li/pccp

1. Introduction

Integrated gasification combined cycle (IGCC), which has higher power generation efficiency compared with traditional coal-fired power plants, is a clean coal power generation technology with future development potential.^{1,2} In the gasification process, coal reacts with an oxidant and water vapor under high temperature and high pressure, producing a mixture of gas components including CO, H₂, H₂O, CO₂, and CH₄. However, some trace elements (such as arsenic and mercury) are volatilized during this process and are subsequently released into the atmosphere, causing environmental pollution and endangering human health.^{3,4} Therefore, it is critical to

design a high-performance adsorbent to remove As and Hg from the effluent gases of the IGCC.

It is known that As₂, As₄, AsO and AsH₃ are the main forms of arsenic pollutants that are present in coal gasification.^{5–7} In particular, the high volatility and toxicity of arsine (AsH₃) have caused widespread concern. Air contaminated with AsH₃ can enter the human body through the respiratory tract and skin, and wastewater containing arsenic can enter the soil and accumulate in crops.^{3,8,9} On the other hand, Hg⁰ is the dominant form of mercury during coal gasification and has adverse effects on the environment and human health.^{10–12} Several adsorbents for arsenic and Hg⁰ removal have been investigated including alloys,^{13–15} noble metals,^{16–18} metal oxides,^{19,20} metal clusters,^{21,22} and other adsorbents.²³ However, these adsorbents have shortcomings associated with their complicated synthesis, high costs, and low efficiency, hindering their widespread application in IGCC facilities.

Recently, single-atom catalysts (SACs) with high metal utilization, where the metal atom with unsaturated coordination acts as the reactive site, have shown great potential for use in the field of heterogeneous catalysis.²⁴ Moreover, the metal

^a Department of Power Engineering, School of Energy, Power and Mechanical Engineering, North China Electric Power University, Baoding 071003, China

^b CNOOC Research Institute of Refining and Petrochemicals, Beijing, 102200, P. R. China. E-mail: wuchch6@cnooc.com.cn

^c Department of Electrical Engineering, North China Electric Power University, Baoding 071003, China

† Electronic supplementary information (ESI) available: Tables S1–S5 and Fig. S1–S4. See DOI: <https://doi.org/10.1039/d1cp02170b>

atom of the SACs can act as the active site for the adsorption of pollutants.^{25,26} As described in previous studies, arsenic pollutants in flue gases are adsorbed on the surface of adsorbents first and then the arsenic oxidation occurs at activated sites.^{27,28} The initial adsorption of arsenic species on adsorbents is a fundamental step to induce the catalytic oxidation of arsenic. In addition to acting as the adsorbent, SACs can also be used directly as the catalysts for subsequent dearsenicization reactions.²⁹ Therefore, adopting suitable single-atom catalysts as adsorbents can not only adsorb arsenic directly, but also lay the foundation for the subsequent dearsenic reaction, making it necessary to explore promising SACs for the adsorption of arsenic pollutants.

Numerous studies have been performed to investigate the adsorption characteristics of toxic gas molecules on single-atom catalysts with vacant graphene substrates: Tang *et al.*^{30,31} studied the adsorption behaviors of Co and Fe anchored on graphene sheets toward NO, SO₂, CO and HCN molecules. Gao *et al.*²⁶ investigated Hg⁰ adsorption on single-atom transition metal (V, Cr, Mn, Co) decorated graphene substrates by density functional theory (DFT) simulations and proved that the Co decorated single vacancy graphene substrate doped with three nitrogen atoms (SV-N₃) was most conducive to the adsorption of Hg⁰ compared with other candidates. According to the study by Yang *et al.*,³² Hg⁰ could be stably adsorbed on four kinds of single atom iron adsorbents supported with graphene-based substrates (Fe/GS). Fe/GS of single vacancy with three nitrogen atoms doped (Fe/SV-N₃) has the best adsorption effect as determined using the density of states (DOS). Yang *et al.*³³ explored the adsorption characteristics of As₂O₃, Pb⁰, PbO and PbCl₂ on the surface of single atom iron adsorbents supported with graphene-based substrates through DFT calculations. Fe/SV-N₃ shows the most excellent adsorption capacity, the adsorption belongs to stable chemisorption, and the adsorption can take place spontaneously when the temperature is below 700 K. Moreover, the competitive adsorption behaviors of Hg⁰, As₂O₃, Pb⁰, PbO, and PbCl₂ on Fe/SV-N₃ were studied, and the results showed that Fe/SV-N₃ would preferentially adsorb Pb⁰ and PbO.

Although there are many studies on the adsorption of Hg⁰ and Pb,^{26,32,33} a few research has been conducted on the adsorption of As₂, As₄, AsO and AsH₃. In order to explore the potential of the simultaneous removal of multiple pollutants in exhaust gases from the IGCC coal plants, we investigated

single-atom Fe supported on nitrogen-doped graphene denoted by Fe_{SA}@V_x-N_y, where *x* = single vacancy (s) and double vacancies (d), and *y* = 0, 3, and 4 N atoms, as adsorbent materials for As₂, As₄, AsO and AsH₃ using DFT computations in this work. The adsorption process is characterized by the adsorption energy, the change of the bond length, and the amount of Bader charge transfer. The underlying adsorption mechanism was explored *via* projected density of states (PDOS) and electron density difference analyses. In addition, the d-band center theory and Fermi softness analyses were performed to explain the adsorption energy differences of the arsenic pollutants on different Fe_{SA}@V_x-N_y adsorbents. The *ab initio* molecular dynamics (AIMD) simulation was also conducted to explore the adsorption characteristics and competitive adsorption behaviors of As₂, As₄, AsO and AsH₃ on Fe_{SA}@V_x-N_y.

2. Methods

All DFT calculations were carried out using the Vienna *Ab initio* Simulation Package (VASP 5.4.4) with the consideration of spin polarization and van der Waals interactions.³⁴ The Perdew–Burke–Ernzerhof (PBE) functional of the generalized gradient approximation (GGA) and projector augmented wave (PAW) methods were utilized to calculate the electron exchange energy and the interaction between the nucleus and electrons, respectively.^{35,36} The plane-wave basis of the kinetic energy cut-off was chosen as 500 eV and Gaussian smearing was 0.05 eV. The theoretical adsorbent model was based on a 4 × 4 graphene supercell with a vacuum layer of 15 Å, which was enough to separate the periodic images of the model along the *z*-direction. A 7 × 7 × 1 *Γ*-centered *k*-point mesh was used with the conjugate-gradient algorithm to optimize the structure with a convergence criterion of 0.02 eV Å⁻¹ in consideration of both the calculation accuracy and time. To obtain accurate energy and electronic properties such as the DOS and magnetic moment, a 15 × 15 × 1 *Γ*-centered *k*-point mesh was adopted to sample the Brillouin zone, and the energy difference should be less than 1 × 10⁻⁵ eV during the calculation of the self-consistent field. All these parameters are consistent with previous studies to ensure the reliability of the results.^{33,37}

To measure the interaction between Fe and substrates, the binding energy (*E_b*) was calculated based on the following equation:

$$E_b = E_{\text{sub+Fe}} - E_{\text{sub}} - E_{\text{Fe}}, \quad (1)$$

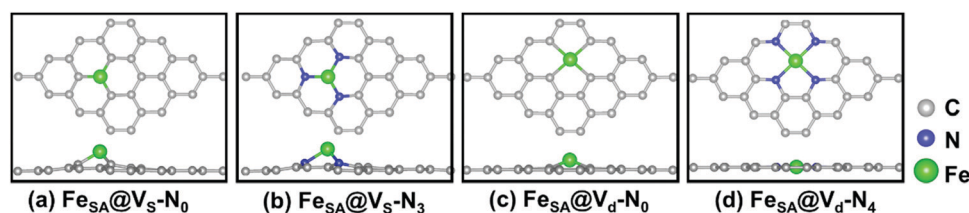


Fig. 1 Geometries of Fe_{SA}@V_x-N_y adsorbents. (a) Fe-modified single vacancy graphene substrate with no nitrogen atom, (b) Fe-modified single vacancy graphene substrate with three nitrogen atoms, (c) Fe-modified double vacancies graphene substrate with no nitrogen atom, (d) Fe-modified double vacancies graphene substrate with four nitrogen atoms.

where $E_{\text{sub+Fe}}$, E_{sub} , and E_{Fe} are the energies of the adsorbent, defective graphene, and the Fe atom, respectively.

Adsorption energy is one of the most well-known tools for evaluating the strength of the interaction between the adsorbate and adsorbent. The adsorption energy (E_{ads}) was calculated by

$$E_{\text{ads}} = E_{\text{sub+adsorbate}} - E_{\text{sub}} - E_{\text{adsorbate}}, \quad (2)$$

where $E_{\text{sub+adsorbate}}$, E_{sub} , and $E_{\text{adsorbate}}$ are the total energy of the system after adsorption, the energy of the adsorbent, and the energy of the adsorbate, respectively.

3. Results and discussion

3.1 Adsorbent models

The geometric models of $\text{Fe}_{\text{SA}}@V_x\text{-N}_y$ are plotted in Fig. 1: (a) and (b) display the Fe-modified single vacancy graphene substrates with no nitrogen atoms and three nitrogen atoms, respectively, whereas (c) and (d) show the Fe-modified double vacancy graphene substrates with no nitrogen atoms and four nitrogen atoms, respectively. The key parameters of the adsorbents such as the bond length, charge transfer, magnetic moment, and binding energy are listed in Table S1 (ESI[†]).³²

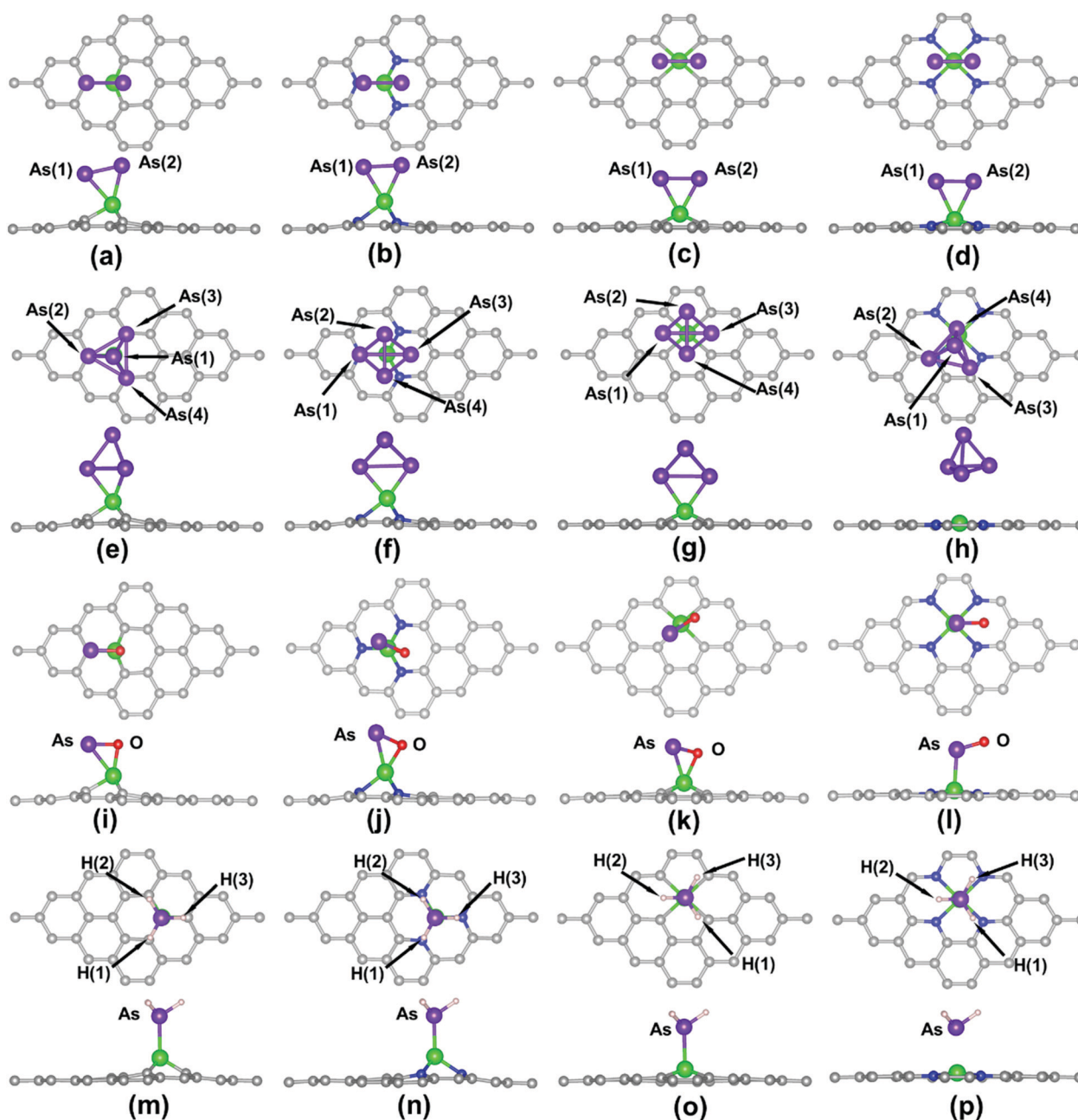


Fig. 2 Optimized structures of As_2 (a)–(d), As_4 (e)–(h), AsO (i)–(l) and AsH_3 (m)–(p) adsorbed on $\text{Fe}_{\text{SA}}@V_x\text{-N}_y$.

As shown in Table S1 (ESI[†]), the binding energy of $\text{Fe}_{\text{SA}}@V_s\text{-N}_3$ is -4.41 eV, and the value is larger than the cohesive energy of Fe (4.28 eV),^{38,39} proving the stability of $\text{Fe}_{\text{SA}}@V_s\text{-N}_3$ by DFT simulation. In addition, the stability of $\text{Fe}_{\text{SA}}@V_s\text{-N}_3$ can be confirmed by charge density difference analysis. According to our previous study,³³ the reduction of the charge density occurred in the vicinity of Fe and its neighboring C atoms, and the accumulation of the charge density occurred near the Fe-C

bond. This obvious electron transfer indicates that a stable chemical bond was formed between the Fe atom and its neighboring C atoms, which can further confirm the stability of $\text{Fe}_{\text{SA}}@V_s\text{-N}_3$. Some experimental results also verified the stability of $\text{Fe}_{\text{SA}}@V_s\text{-N}_3$. In a study by Haidong Yang *et al.*,⁴⁰ the Fe single-atom catalyst anchored on the nitrogen-doped carbon substrates (including $\text{Fe}_{\text{SA}}@V_s\text{-N}_3$ and $\text{Fe}_{\text{SA}}@V_d\text{-N}_4$) was prepared and stability tests confirmed that $\text{Fe}_{\text{SA}}@V_s\text{-N}_3$ and

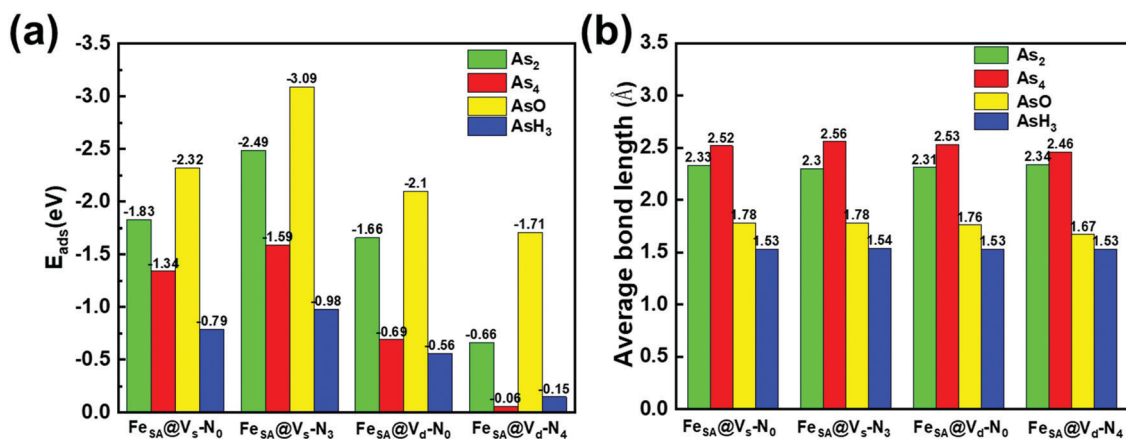


Fig. 3 (a) Adsorption energies and (b) the average bond lengths of As_2 , As_4 , AsO and AsH_3 on $\text{Fe}_{\text{SA}}@V_x\text{-N}_y$.

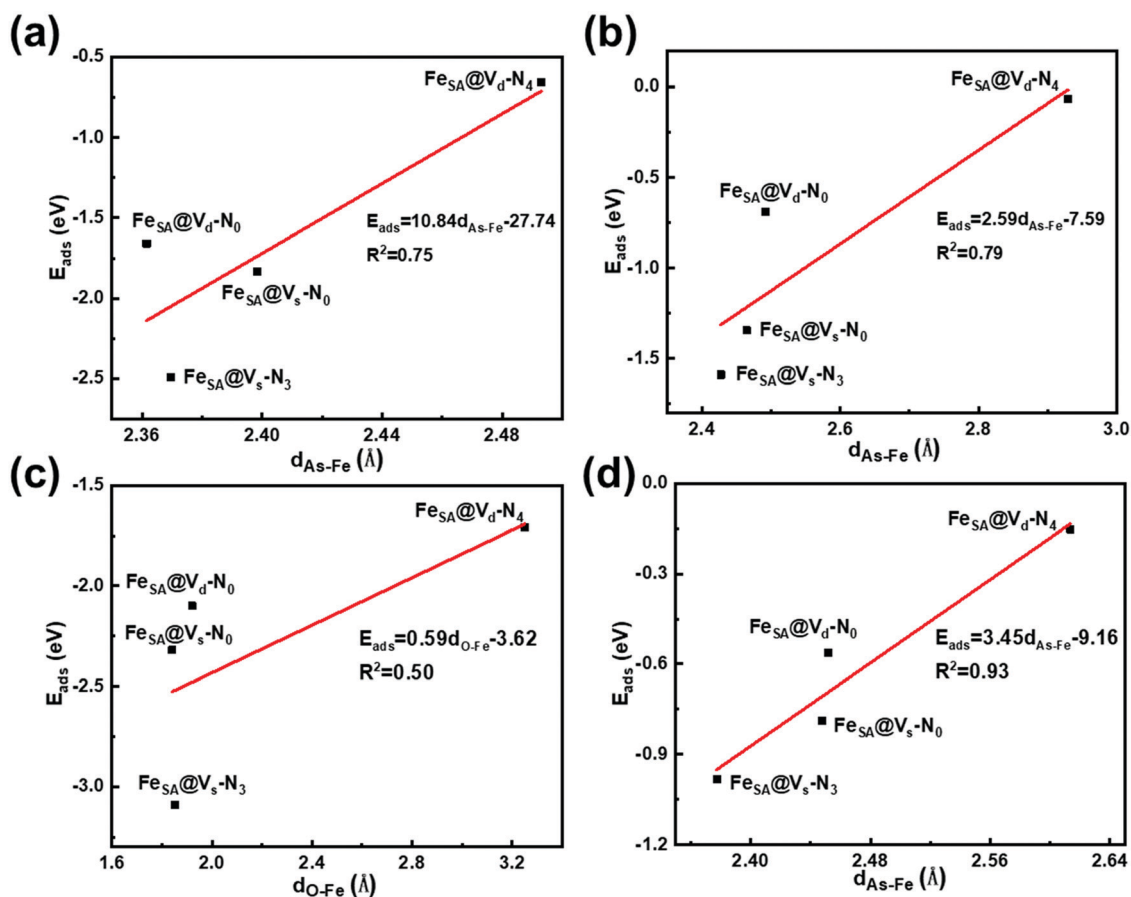


Fig. 4 Linear relationships between $d_{\text{As-Fe}}$ ($d_{\text{O-Fe}}$ for AsO) and adsorption energies of (a) As_2 , (b) As_4 , (c) AsO and (d) AsH_3 .

$\text{Fe}_{\text{SA}}@V_{\text{d}}\text{-N}_4$ are highly stable. In addition, Robertson *et al.*⁴¹ also prepared and proved the stability of the Fe decorated graphene substrate doped with nitrogen atoms.

3.2 Adsorption of As_2 , As_4 , AsO , and AsH_3

Two typical adsorption modes (end-on and side-on configurations) were adopted for As_2 to obtain the most stable adsorption structure as shown in Fig. S1(a) and (b) (ESI[†]). The end-on configuration is the case where As_2 adsorbs almost perpendicularly on the graphene substrate to form a single As-Fe bond. On the other hand, the side-on configuration is a parallel adsorption mode, where As_2 interacts with the Fe atom to form two bonds. The E_{ads} of the end-on and side-on configurations for As_2 are shown in Fig. S2 (ESI[†]), which reveals that As_2 is more likely to be adsorbed on $\text{Fe}_{\text{SA}}@V_{\text{x}}\text{-N}_y$ in the side-on configuration because of the more negative adsorption energy.

After structural optimization, the most stable structure of As_2 adsorbed on $\text{Fe}_{\text{SA}}@V_{\text{x}}\text{-N}_y$ in the side-on mode is shown in Fig. 2(a)–(d). The Bader charge transfers of Fe (Δq_{Fe}), As_2 (Δq_{As_2}), and support (Δq_{Gra}), the bond lengths of As_2 (As(1)–As(2)) and As–Fe (As(1)–Fe and As(2)–Fe), and the magnetic moment of the system (M) after adsorption are listed in Table S2 (ESI[†]). Similarly, three possible adsorption configurations of As_4

on $\text{Fe}_{\text{SA}}@V_{\text{x}}\text{-N}_y$ were examined, as shown in Fig. S3 (ESI[†]). The most stable adsorption structures are presented in Fig. 2(e)–(h) after the structural optimization and comparison of the adsorption energy. The key parameters including the bond length between As atoms in As_4 , the distance between the Fe atom and As atom, the Bader charge transfers of As_4 , Fe atom and substrate, and the magnetic moment are listed in Table S3 (ESI[†]). The geometric structures of AsO and AsH_3 adsorbed on $\text{Fe}_{\text{SA}}@V_{\text{x}}\text{-N}_y$ were optimized with the results shown in Fig. 2(i)–(l) and (m)–(p). The key parameters of the adsorption system are listed in Tables S4 and S5 (ESI[†]), respectively.

The adsorption energies of As_2 , As_4 , AsO , and AsH_3 on $\text{Fe}_{\text{SA}}@V_{\text{x}}\text{-N}_y$ are summarized in Fig. 3(a). From Fig. 3(a), the adsorption energy of As_2 on $\text{Fe}_{\text{SA}}@V_{\text{s}}\text{-N}_3$ is -2.49 eV, which achieves the best performance among all the $\text{Fe}_{\text{SA}}@V_{\text{x}}\text{-N}_y$ adsorbents investigated here. The adsorption of As_2 on $\text{Fe}_{\text{SA}}@V_{\text{d}}\text{-N}_4$ is the weakest, which is equal to -0.66 eV. With regard to As_4 , it has the most stable adsorption when being adsorbed on $\text{Fe}_{\text{SA}}@V_{\text{s}}\text{-N}_3$ with an adsorption energy of -1.59 eV. The adsorption energy of As_4 on $\text{Fe}_{\text{SA}}@V_{\text{d}}\text{-N}_4$ is the smallest, which is only -0.06 eV. Similarly, the maximum adsorption energies of AsO and AsH_3 on $\text{Fe}_{\text{SA}}@V_{\text{s}}\text{-N}_3$ are -3.09 eV and -0.98 eV, respectively. $\text{Fe}_{\text{SA}}@V_{\text{d}}\text{-N}_4$ has poor

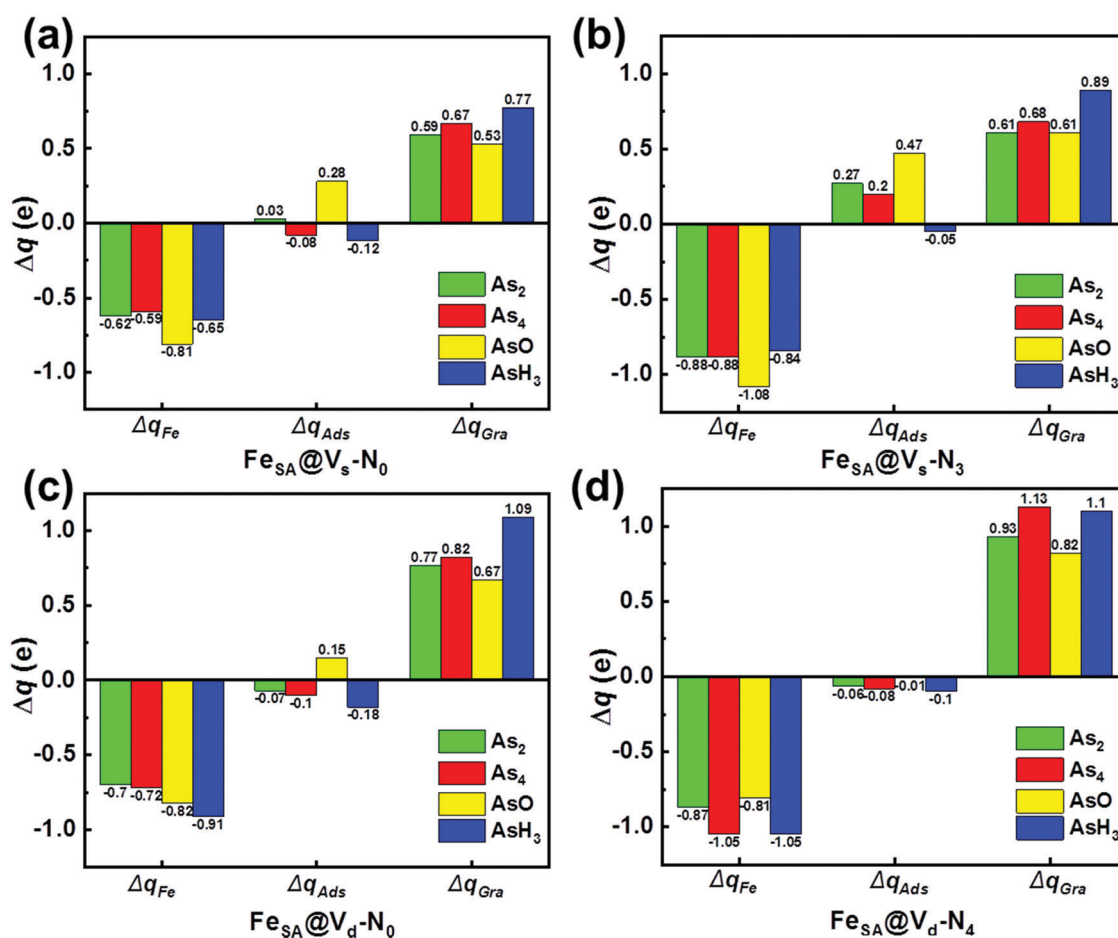


Fig. 5 Electron transfer (Δq) among the adsorbate, Fe, and graphene for 4 substrates: (a) $\text{Fe}_{\text{SA}}@V_{\text{s}}\text{-N}_0$, (b) $\text{Fe}_{\text{SA}}@V_{\text{s}}\text{-N}_3$, (c) $\text{Fe}_{\text{SA}}@V_{\text{d}}\text{-N}_0$, and (d) $\text{Fe}_{\text{SA}}@V_{\text{d}}\text{-N}_4$.

adsorption performance for AsO and AsH₃ with adsorption energies being -1.71 eV and -0.15 eV, respectively. Therefore, Fe_{SA}@V_s-N₃ has the largest adsorption energies toward As₂, As₄, AsO and AsH₃ among the Fe_{SA}@V_x-N_y materials studied here.

The average bond length (the As-As bond for As₂ and As₄, the As-O bond for AsO, and the As-H bond for AsH₃) after adsorption was determined to investigate the adsorption strength from the geometric structure, as shown in Fig. 3(b). The average bond lengths of As-As for adsorbed As₂ and As₄ exceed to 2.30 Å and 2.46 Å, respectively, compared to the isolated As₂ (2.10 Å) and As₄ (2.44 Å).^{42,43} The bond length of As-O exceeds to 1.67 Å compared to the isolated AsO (1.62 Å).⁴⁴ The bond length of As-H does not change significantly compared to the isolated AsH₃ (1.52 Å).⁴⁵ Given the change of the bond length, it can be speculated that As₂, As₄ and AsO are activated by Fe_{SA}@V_x-N_y.

Gao²⁶ found that there was a linear relationship between the adsorption energy and the distance of the adsorbate and the active center. Therefore, the relationships between the distance of Fe and As atoms ($d_{\text{Fe-As}}$) and the adsorption energies of As₂, As₄, and AsH₃ were explored and are shown in Fig. 4(a), (b) and (d), respectively. The results reveal that there is a positive correlation between $d_{\text{Fe-As}}$ and the adsorption energies of As₂,

As₄, and AsH₃, and the square of the correlation coefficients are 0.75, 0.79, and 0.93, respectively, indicating that $d_{\text{Fe-As}}$ provides a means to characterize the adsorption energy. For AsO, the relationship between the adsorption energy and $d_{\text{Fe-As}}$ does not seem to follow this rule, but there is some kind of weak correlation between the adsorption energy and $d_{\text{Fe-O}}$, as shown in Fig. 4(c).

Bader charge analysis was performed to characterize the charge transfer of each part after adsorption, as shown in Fig. 5(a)–(d). In all the adsorption processes, the Fe atoms act as electron donors and the substrate gains electrons. In Fig. 5(a), As₂ and AsO gain electrons when being adsorbed on Fe_{SA}@V_s-N₀ (+0.03 e and +0.27 e, respectively), while As₄ and AsH₃ lose electrons to Fe_{SA}@V_s-N₀ (-0.08 e and -0.12 e). As₂, As₄, and AsO gain electrons from Fe_{SA}@V_s-N₃ (+0.27 e, +0.20 e and +0.47 e, respectively), and AsH₃ loses electrons to Fe_{SA}@V_s-N₃ (-0.05 e). On the other hand, AsO gains electrons from Fe_{SA}@V_d-N₀ (+0.15 e), while As₂, As₄, and AsH₃ lose electrons to Fe_{SA}@V_d-N₀ (-0.07 e, -0.10 e and -0.18 e, respectively). With regard to Fe_{SA}@V_d-N₄, all the adsorbates lose electrons to the substrate (-0.06 e, -0.08 e, -0.01 e, and -0.10 e, respectively). The electrons obtained for As₂, As₄, and AsO during the adsorption process occupy the antibonding orbitals of As₂,

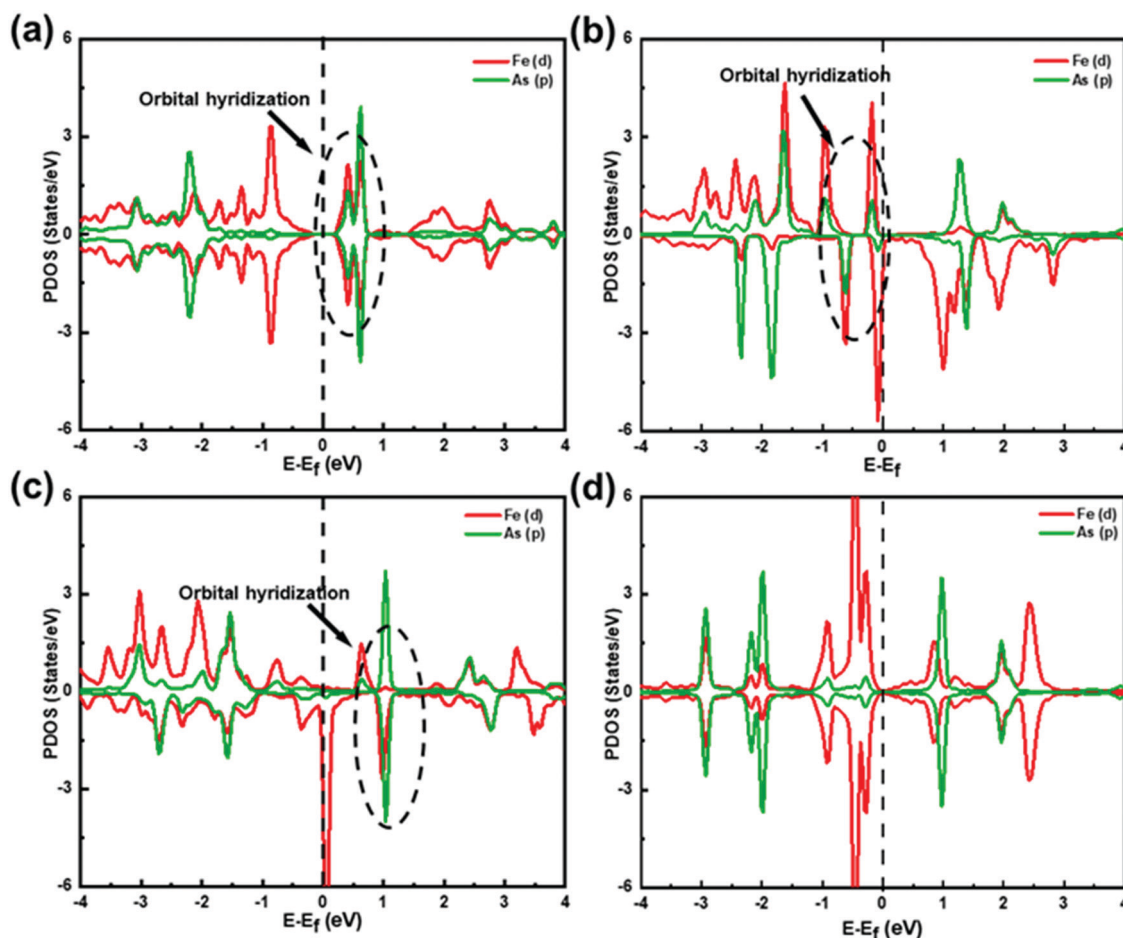


Fig. 6 PDOS of Fe_{SA}@V_x-N_y after As₂ adsorption. (a)–(d) The PDOS of Fe_{SA}@V_s-N₀, Fe_{SA}@V_s-N₃, Fe_{SA}@V_d-N₀, and Fe_{SA}@V_d-N₄, respectively.

As₄, and AsO, which may account for the greater adsorption energy of the Fe_{SA}@V_s-N₃ adsorbent. Furthermore, for all the Fe_{SA}@V_x-N_y cases, AsH₃ always loses electrons in the adsorption process due to the lowest electronegativity of AsH₃ among the four species.

3.3 Electronic and magnetic property analyses

To further understand the adsorption energies of As₂, As₄, AsO and AsH₃ on Fe_{SA}@V_x-N_y, the electronic and magnetic properties were analyzed. First, PDOS after As₂, As₄, AsO and AsH₃ adsorption was used to analyze the orbital hybridization. The PDOS of Fe_{SA}@V_x-N_y after As₂, As₄, AsO and AsH₃ adsorption is shown in Fig. 6–9, respectively. In Fig. 6, the DOS of the d orbital of Fe is drawn with the red line, and that of the p orbital of As is drawn using the green line. The bonding mechanism of As₂, As₄ and AsO adsorbed on Fe_{SA}@V_x-N_y may be the same given the similar PDOS profiles displayed in Fig. 6–8. From Fig. 6(a)–(c), 7(a)–(c) and 8(a)–(c), there is an obvious hybrid peak between Fe (d) and As (p) near the Fermi level, indicating that there is a contribution of orbital hybridization during the bonding process of As₂, As₄ and AsO on Fe_{SA}@V_s-N₀, Fe_{SA}@V_s-N₃, and Fe_{SA}@V_d-N₀. However, there is no obvious hybrid peak between Fe (d) and As (p) near the Fermi level in Fig. 6(d),

7(d) and 8(d), implying that the contribution of orbital hybridization can be neglected in these adsorption processes. For the PDOS of AsH₃ adsorbed on Fe_{SA}@V_x-N_y, there is no hybrid peak in Fig. 9(a)–(d), indicating that there is no orbital hybridization contribution during the bonding process of AsH₃. For As₂, As₄ and AsO, the adsorption energies of these molecules can be well understood by orbital hybridization. As we all know, the Fermi level can indicate whether there are electrons in the orbitals. When the hybridization occurs for $E < E(\text{Fermi})$, there will be electrons occupied in the hybrid orbitals, indicating that the binding interaction is strong, corresponding to a large adsorption energy. When the hybridization occurs for $E > E(\text{Fermi})$, there will be no electrons occupied in the hybrid orbitals, indicating that the promotion effect of hybridization on the binding strength is relatively weak, corresponding to a medium adsorption energy. If there is no hybridization, no promotion effect of hybridization exists on the binding strength, indicating that the binding strength is weak, corresponding to a small adsorption energy. The magnetic moment of the system after adsorption was calculated and is listed in Tables S2–S5 (ESI[†]). The results demonstrate that the magnetic moment of the Fe_{SA}@V_s-N₀ system after As₂, As₄, and AsH₃ adsorption, the Fe_{SA}@V_d-N₀ system after AsO

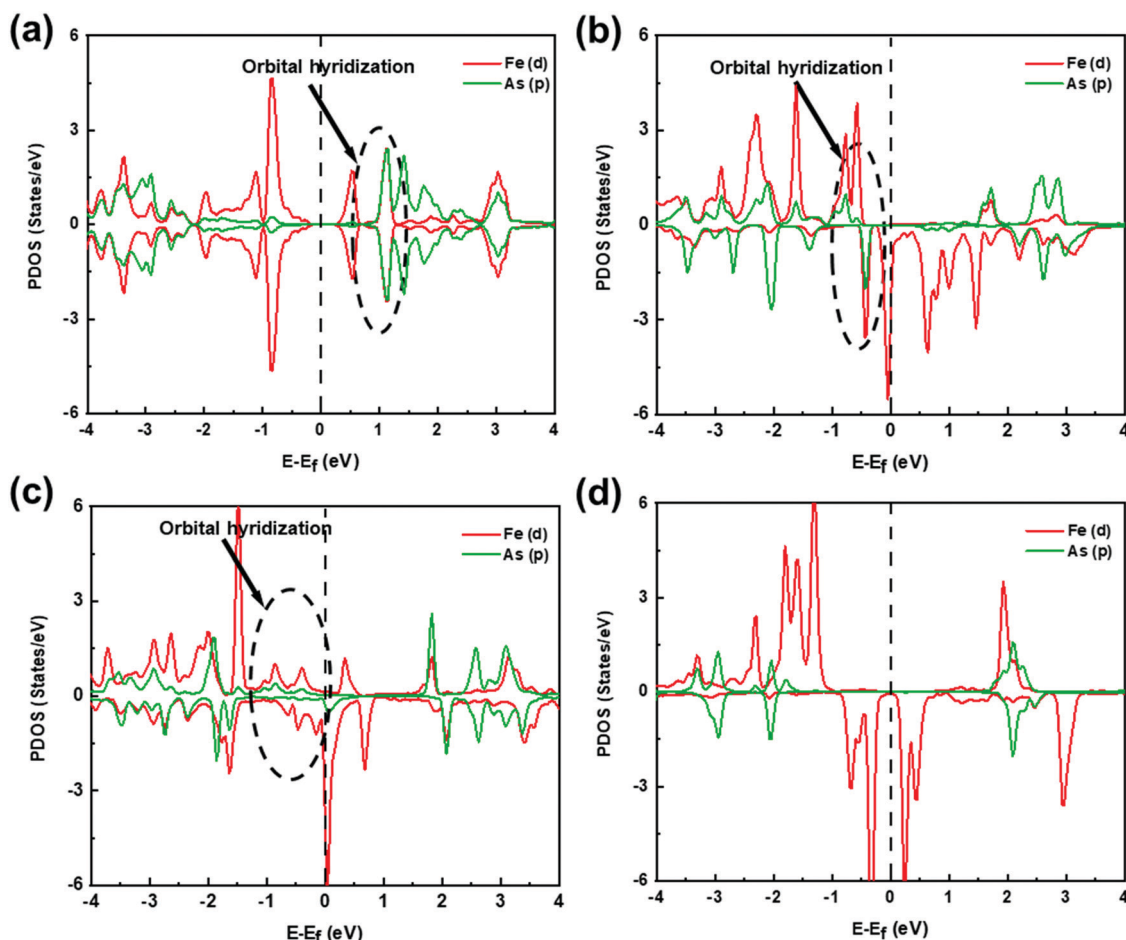


Fig. 7 PDOS of Fe_{SA}@V_x-N_y after As₄ adsorption. (a)–(d) The PDOS of Fe_{SA}@V_s-N₀, Fe_{SA}@V_s-N₃, Fe_{SA}@V_d-N₀, and Fe_{SA}@V_d-N₄, respectively.

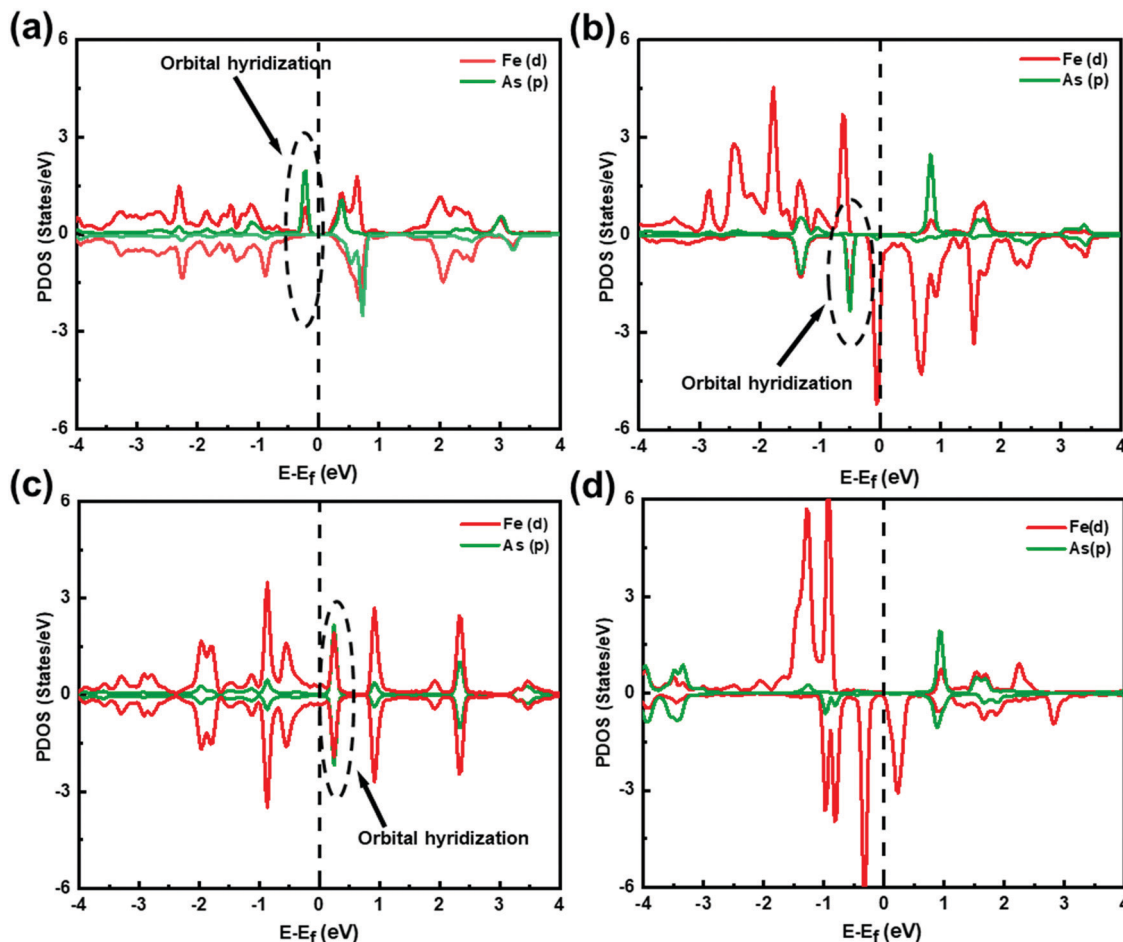


Fig. 8 PDOS of $\text{Fe}_{\text{SA}}@V_x\text{-N}_y$ after AsO adsorption. (a)–(d) The PDOS of $\text{Fe}_{\text{SA}}@V_s\text{-N}_0$, $\text{Fe}_{\text{SA}}@V_s\text{-N}_3$, $\text{Fe}_{\text{SA}}@V_d\text{-N}_0$, and $\text{Fe}_{\text{SA}}@V_d\text{-N}_4$, respectively.

adsorption and the $\text{Fe}_{\text{SA}}@V_d\text{-N}_4$ system after As_2 adsorption are zero. This is consistent with Fig. 6(a), (d), 7(a), 8(c), 9(a) because the density state of their spin up and down is symmetrical.

To investigate the electron transfer between the adsorbate (As_2 , As_4 , AsO and AsH_3) and substrate in the bonding process visually, the electron density difference (EDD) images are plotted and shown in Fig. 10. The electron density difference ($\Delta\rho$) is defined as follows:

$$\Delta\rho = \rho_{\text{sub+adsorbate}} - \rho_{\text{sub}} - \rho_{\text{adsorbate}}, \quad (3)$$

where $\rho_{\text{sub+adsorbate}}$ and ρ_{sub} are the charge density of the $\text{Fe}_{\text{SA}}@V_x\text{-N}_y$ system after and before adsorption, respectively, and $\rho_{\text{adsorbate}}$ is the charge density of As_2 , As_4 , AsO or AsH_3 . The atom coordinates are consistent with the adsorbed $\text{Fe}_{\text{SA}}@V_x\text{-N}_y$ system during the calculation of $\Delta\rho$. Yellow and cyan denote the electron density accumulation and loss regions, respectively. The results in Fig. 10(a)–(d) reveal that the electron density accumulation mainly occurs at the As–Fe bond during the As_2 adsorption process, which is beneficial to strengthen the interaction between the As atom and Fe atom. The electron density is depleted around the As–As bond, which leads to a weaker As–As bond. In Fig. 10(i)–(l), the electron density difference of AsO is similar to that of As_2 : the electron density accumulates at the As–Fe bond,

and the electron density depletes around the As–O bond, which indicates that the interaction of Fe and As atoms is strengthened, while the interaction of As and O atoms is weakened. For the adsorption process of As_4 on $\text{Fe}_{\text{SA}}@V_s\text{-N}_0$, $\text{Fe}_{\text{SA}}@V_s\text{-N}_3$, and $\text{Fe}_{\text{SA}}@V_d\text{-N}_0$, as shown in Fig. 10(e)–(g), the electron density accumulates at the As–Fe bond, strengthening the As–Fe bond. For the $\text{Fe}_{\text{SA}}@V_d\text{-N}_4$ system, there is almost no electron density accumulation at the As–Fe bond, as shown in Fig. 10(h), which corresponds to its weak adsorption energy. The electron density difference of AsH_3 , as shown in Fig. 10(m)–(p), is similar to As_4 : the Fe–As bond is strengthened by the electron density accumulation in $\text{Fe}_{\text{SA}}@V_s\text{-N}_0$, $\text{Fe}_{\text{SA}}@V_s\text{-N}_3$, and $\text{Fe}_{\text{SA}}@V_d\text{-N}_0$. However, in the $\text{Fe}_{\text{SA}}@V_d\text{-N}_4$ system, the electron density accumulation at the As–Fe bond is significantly smaller than that of other systems, which may reduce the adsorption capability. The analysis of the EDD was consistent with the results of the previous Bader charge analysis presented in Fig. 5(a)–(d).

To explore the effect of charge transfer on the bonding mechanism, the relationship between charge transfer and adsorption energy was examined and is shown in Fig. 11. In the adsorption process of As_2 , the charge transfer and adsorption energy have a linear relationship with the square of the correlation coefficient (R^2) equal to 0.65; meanwhile, in

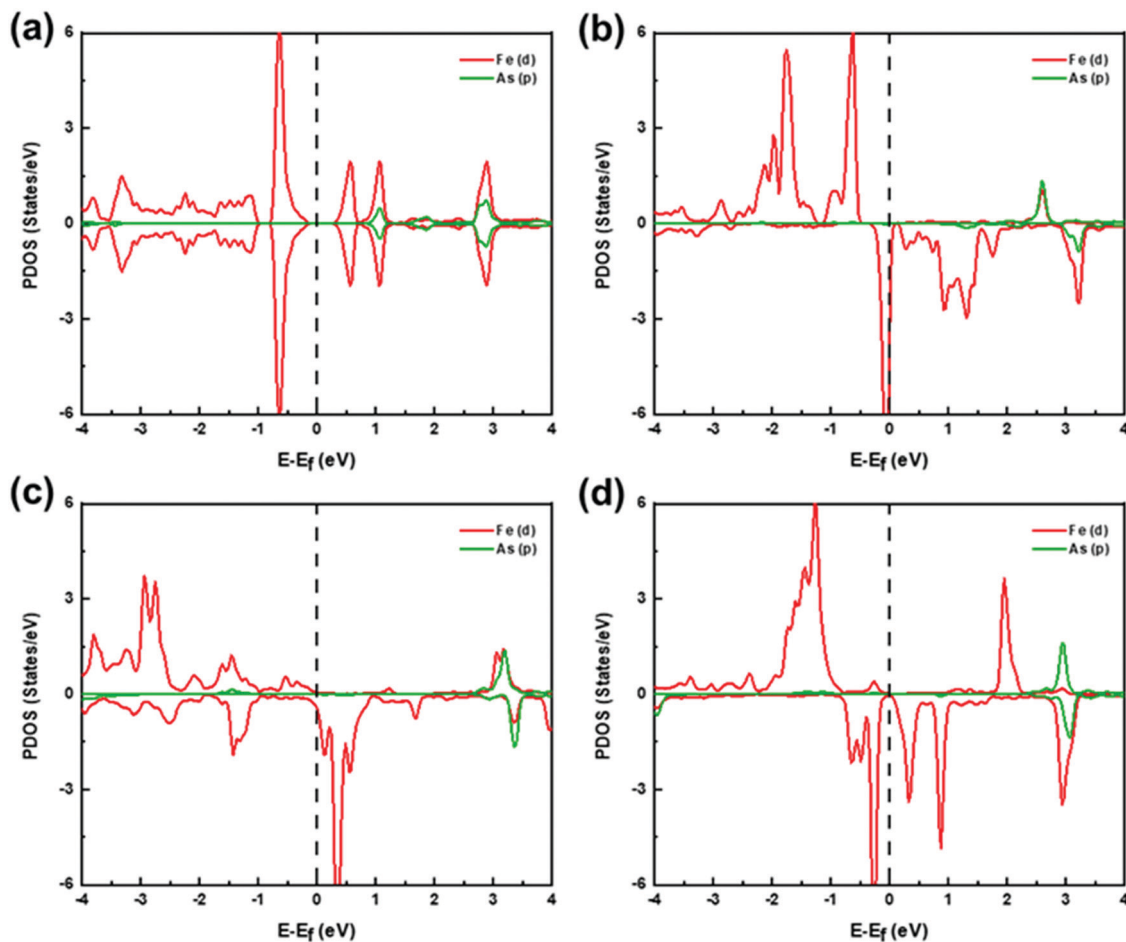


Fig. 9 PDOS of $\text{Fe}_{\text{SA}}@V_x\text{-N}_y$ after AsH_3 adsorption. (a)–(d) The PDOS of $\text{Fe}_{\text{SA}}@V_s\text{-N}_0$, $\text{Fe}_{\text{SA}}@V_s\text{-N}_3$, $\text{Fe}_{\text{SA}}@V_d\text{-N}_0$, and $\text{Fe}_{\text{SA}}@V_d\text{-N}_4$, respectively.

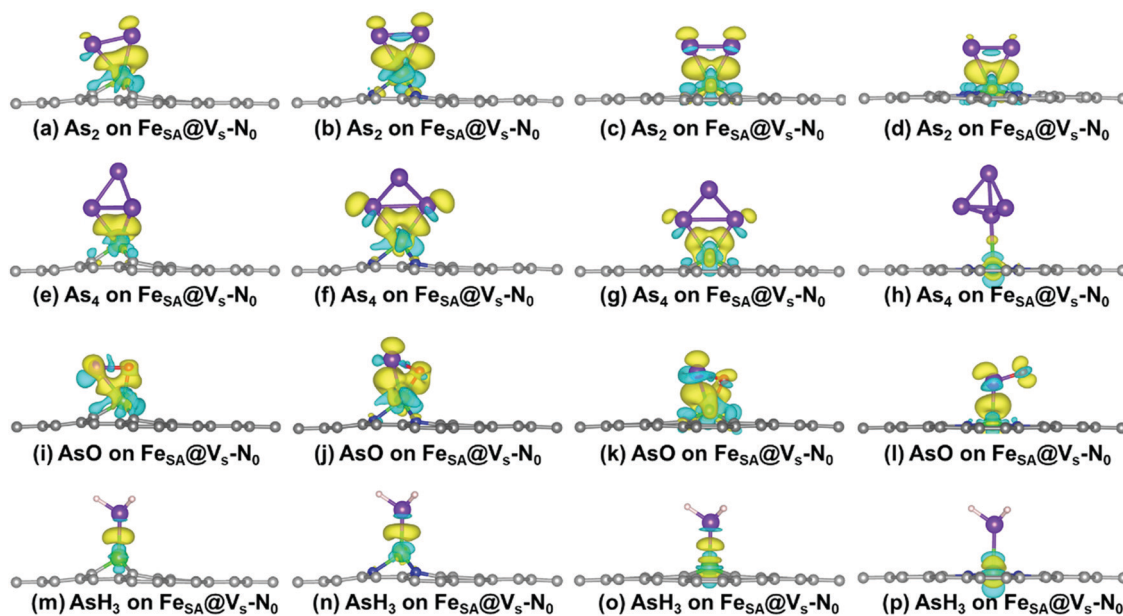


Fig. 10 Electron density differences of As_2 (a)–(d), As_4 (e)–(h), AsO (i)–(l), and AsH_3 (m)–(p). (Contour lines in plots are drawn at $0.004 \text{ e}^- \text{ \AA}^{-3}$ intervals).

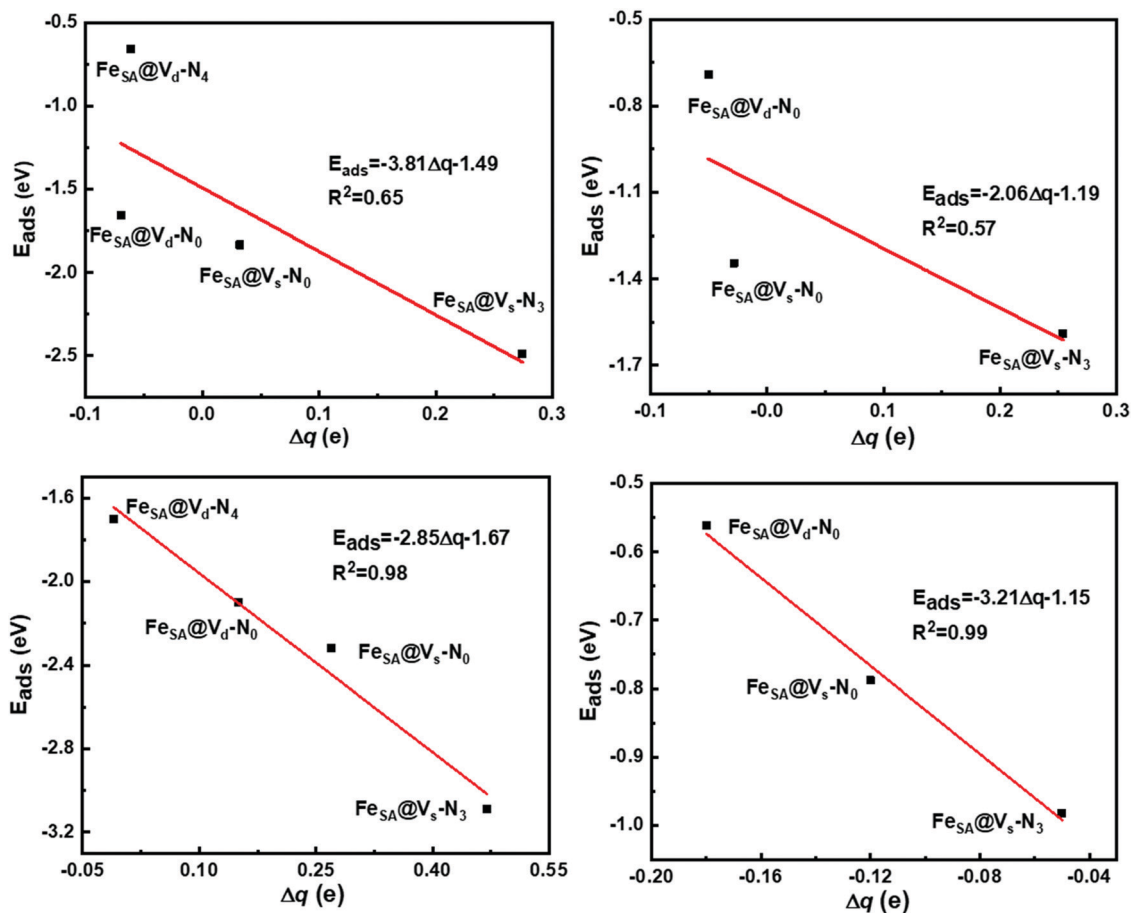


Fig. 11 The relationship between Δq and adsorption energies of (a) As_2 , (b) As_4 , (c) AsO , and (d) AsH_3 .

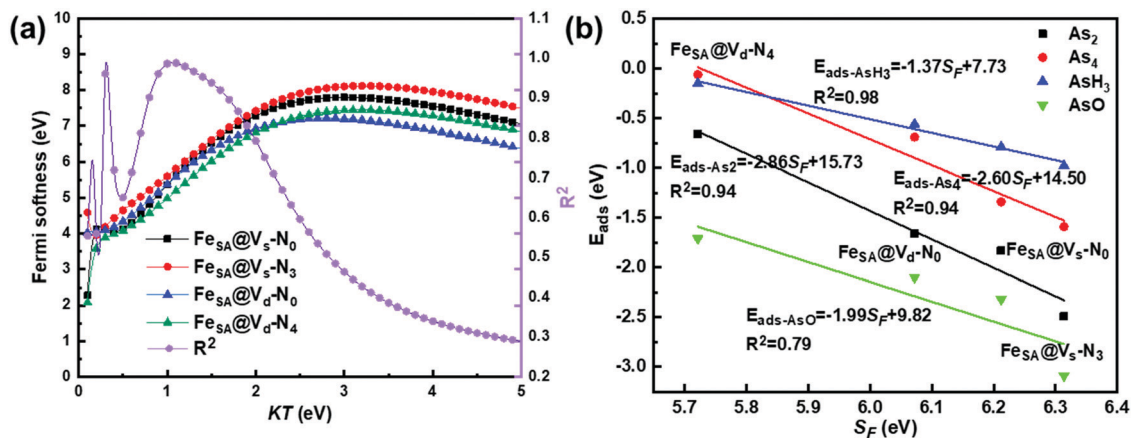


Fig. 12 The effect of kT on S_F and correlation coefficient (a) and (b) adsorption energies of As_2 , As_4 , AsO and AsH_3 as a function of the Fermi softness at $kT = 1.35$ eV.

the process of As_4 adsorption, the square of the correlation coefficient (R^2) of the charge transfer and adsorption is 0.57, suggesting that the charge transfer is not the dominate mechanism for the adsorption of As_2 and As_4 . It is noteworthy that the hybridization peaks for the PDOS of As_2 and As_4 are more obvious than that for AsO and AsH_3 , suggesting that

hybridization plays an important role for the adsorption of As_2 and As_4 on the graphene-based single-atom iron adsorbents. Unlike As_2 and As_4 , the charge transfer has a more important influence on the adsorption process of AsO and AsH_3 . The square of the correlation coefficients (R^2) between the charge transfer and adsorption energy are 0.98 and 0.99, respectively,

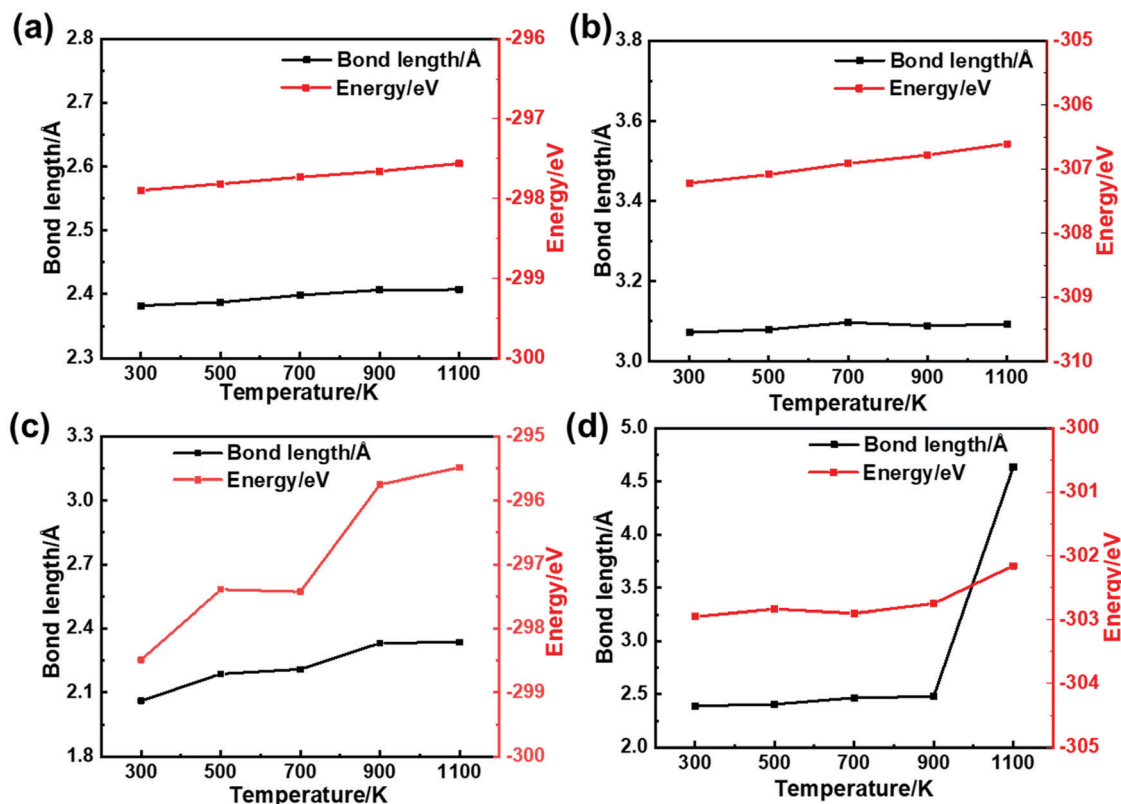


Fig. 13 (a)–(d) Average bond lengths and energies of As₂, As₄, AsO and AsH₃ to the surface under different temperatures through the AIMD simulation.

indicating that the adsorption of AsO and AsH₃ is affected by electronic transfer. There are no Fe_{SA}@V_d-N₄ data for As₄ and AsH₃ because they are physically adsorbed on its surface, which is different from the adsorption of arsenic pollutants by the other adsorbents. According to the above PDOS and EDD analyses, both charge transfer and orbital hybridization affects the adsorption processes of As₂, As₄, and AsO, while only charge transfer plays a dominant role in the adsorption process of AsH₃.

Based on our previous research conclusions,^{32,33} the adsorption energies of Pb⁰, PbO, PbCl₂, Hg⁰, HgCl, HgCl₂, As₂O₃, As₂, As₄, AsO and AsH₃ on the Fe_{SA}@V_s-N₃ system are -2.15, -2.83, -1.89, -0.81, -2.13, -2.23, -2.20, -2.49, -1.59, -3.09 and -0.98 respectively, indicating that they are all chemisorption. Therefore, there is a great potential for Fe_{SA}@V_s-N₃ to remove multiple pollutants in the IGCC flue gases, such as the pollutants of mercury, lead and arsenic.

3.4 Electronic structure analysis

Different substrates cause the same adsorbate to have different adsorption energies, namely, different coordination environments of Fe lead to different adsorption energies of the same adsorbate. Therefore, it is necessary to explore the differences of the substrates to reveal how the coordination environment affects the adsorption process. In this section, *d*-band center theory and Fermi softness are used to investigate the impact of the Fe coordination environment.

The *d*-band center theory is widely used to characterize the activity of transition metals on various solid surfaces (such as

pure metal surfaces,^{46,47} alloys,^{48,49} and metallic organic frameworks^{50,51}). Therefore, it is necessary to investigate whether the *d*-band center is suitable for the analysis of Fe_{SA}@V_x-N_y. The *d*-band center, (ϵ_d), of Fe_{SA}@V_x-N_y was calculated according to the pioneering research of Norskov:⁴⁶

$$\epsilon_d = \frac{\int_{-}^{+} E \cdot D(E) dE}{\int_{-}^{+} D(E) dE} \quad (4)$$

where $D(E)$ is the *d* orbital states of the Fe atom in Fe_{SA}@V_x-N_y. The calculated *d*-band center values for Fe_{SA}@V_s-N₀, Fe_{SA}@V_s-N₃, Fe_{SA}@V_d-N₀, and Fe_{SA}@V_d-N₄ are -0.97 eV, -1.85 eV, -1.17 eV, and -1.15 eV, respectively. The adsorption activity order of Fe_{SA}@V_x-N_y is Fe_{SA}@V_s-N₀ > Fe_{SA}@V_d-N₄ ≈ Fe_{SA}@V_d-N₀ > Fe_{SA}@V_s-N₃ according to the *d*-band center value, which is inconsistent with the adsorption activity order calculated from the adsorption energy. There is no linear relationship between the adsorption energy and *d*-band center, implying that the *d*-band center is not a suitable descriptor for adsorption energy in this study.

Based on the frontier molecular orbital theory, the whole frontier electronic band of the solid surface influences the active site. The electronic states near the Fermi level are more likely to participate in the bonding process, and therefore impacting the reaction process. The Fermi softness can comprehensively investigate the contribution of the whole frontier electronic band of the solid surface from the electronic states and the degree close to the Fermi level. The Fermi softness (S_F) is derived from the DOS, $g(E)$,

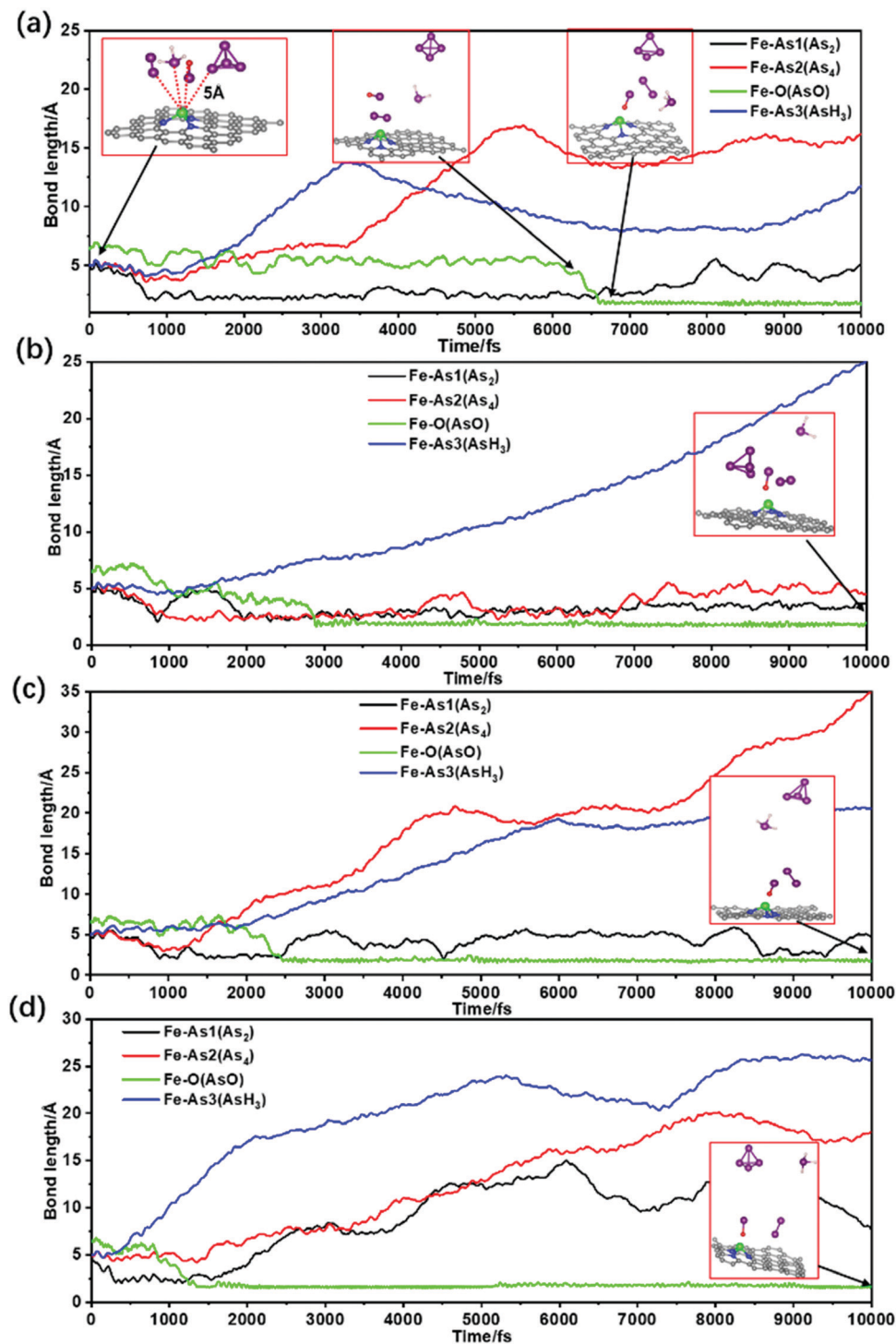


Fig. 14 Competitive adsorption behaviors between As_2 , As_4 , AsO and AsH_3 through AIMD simulations. (a) 300 K, (b) 500 K, (c) 700 K and (d) 900 K.

and the weight function, $W(E)$, and is defined as⁵²

$$S_F = - \int_{-}^{+} g(E) \cdot W(E) dE \quad (5)$$

where $g(E)$ is the total DOS and $W(E)$ is determined by the derivative of the Fermi-Dirac function: $-f_T'(E - E_F)$.

The Fermi-Dirac function is defined as

$$f_T'(E - E_F) = \frac{1}{kT} \cdot \frac{1}{(e^{(E-E_F)/kT} + 1)(e^{(E_F-E)/kT} + 1)} \quad (6)$$

where k is the Boltzmann constant and T is the parametric temperature. The relationship between the Fermi softness of $\text{Fe}_{\text{SA}}@V_{\text{x-N}_y}$ and the corresponding adsorption energy is related

to kT based on a previous study.^{52,53} Therefore, the Fermi softness value of the adsorbent was calculated from $kT = 0.1$ to 5 eV with the results shown in Fig. 12(a). The Fermi softness of $\text{Fe}_{\text{SA}}@V_x\text{-N}_y$ increases first and then decreases gradually. The R^2 between S_F and adsorption energy changes a lot *versus* kT , indicating that the selection of kT has a great influence on the Fermi softness. The results show that R^2 increases first and then decreases with the increase of kT when $kT > 0.5$. When kT is around 1.35 eV, the square of the correlation coefficient (R^2) reaches the maximum value, which is consistent with a previous study.³² The correlation between the Fermi softness and adsorption energy is plotted in Fig. 12(b) at $kT = 1.35$ eV. From Fig. 12(b), R^2 between S_F and the adsorption energies of As_2 , As_4 , AsO and AsH_3 are 0.94, 0.94, 0.79 and 0.98, respectively. Obviously, S_F can be used as a valid descriptor of the adsorption energy. The correlation coefficient of AsO is lower than those of AsH_3 , As_2 , and As_4 due to the electrostatic interactions that AsO participates in.

3.5 AIMD simulations

To further testify the binding strength of $\text{Fe}_{\text{SA}}@V_s\text{-N}_3$ for As_2 , As_4 , AsO and AsH_3 , the average bond lengths (the average of the distance between each atom of the adsorbates and the surface) and energy between adsorbates and surface were calculated through AIMD simulations at 300 to 1100 K, as shown in Fig. 13(a)–(d). Each AIMD simulation was performed at a relatively long time of 10 ps with a time step of 1 fs. With the increase of temperature, the bond lengths and energy increase in a small range as shown in Fig. 13(a)–(c), corresponding to the final adsorption structures of Fig. S4(a)–(c) (ESI[†]), which indicates that the adsorption systems of As_2 , As_4 and AsO are relatively stable. Nevertheless, the bond lengths and energy have a large fluctuation for AsH_3 at 1100 K (Fig. 13(d)), demonstrating a greater change for the AsH_3 adsorption system. It is further explained by the desorption of AsH_3 at 1100 K in Fig. S4(d) (ESI[†]). It is concluded that As_2 , As_4 and AsO can be stably adsorbed when the temperature is below 1100 K, while AsH_3 would desorb between 900 and 1100 K, and the adsorption capacity is consistent with the adsorption energy and bond mechanisms from the DFT calculation.

Considering that there was a competitive adsorption between four molecules, As_2 , As_4 , AsO and AsH_3 were added to the same simulation system to study their competitive adsorption behaviors. All the initial distances between the Fe atom and As atom in four molecules are 5 Å, as shown in Fig. 14(a). At 300 K, the competitive adsorption behaviors in 10 ps is shown in Fig. 14(a); at the beginning, four molecules compete for adsorption sites, AsH_3 and As_4 gradually move away from the adsorption site subsequently, and As_2 has an advantage in competition with AsO before 6500 fs; but, from about 6500 fs, As_2 is gradually replaced by AsO and then AsO occupies the adsorption site until 10 000 fs. The configurations of the four molecules at 6400 fs and 6600 fs are also shown in Fig. 14(a); there is an obvious difference in the arrangement of the molecules in the two configurations, which also means the change in the adsorption capacity. Similarly, at

500 K (Fig. 14(b)), As_2 , AsO and As_4 have a competitive relationship, at 700 K (Fig. 14(c)), and As_2 and AsO compete for adsorption sites; but AsO seems to have stronger adsorption capacity in the two cases, and the configuration of the final step is also shown in their respective figure. At 900 K (Fig. 14(d)), there is a competition for adsorption sites between As_2 and AsO before 1200 fs, and AsO occupies the adsorption sites stably in the end. Overall, in this adsorption competition modeling at 300 to 900 K, it is mainly the competitive adsorption between AsO and As_2 , and AsO is more competitive for adsorption sites, which is consistent with the highest adsorption energy of AsO .

4. Conclusions

The potential of $\text{Fe}_{\text{SA}}@V_x\text{-N}_y$ for the adsorption of As_2 , As_4 , AsO and AsH_3 , and competitive adsorption behaviors were systematically investigated based on the DFT and AIMD calculations. Among all the adsorbents, the adsorption energies of As_2 , As_4 , AsO and AsH_3 by $\text{Fe}_{\text{SA}}@V_s\text{-N}_3$ are the highest. The bonding mechanism of As_2 , As_4 and AsO consists of charge transfer and orbital hybridization. The $\text{Fe}_{\text{SA}}@V_s\text{-N}_3$ system has the most obvious hybridization peaks with As_2 , As_4 and AsO and has the largest amount of transferred charge, resulting in the largest adsorption energy. In the adsorption process of AsH_3 , the bonding mechanism was mainly affected by charge transfer. Compared with the d-band center theory, Fermi softness is a more suitable descriptor for characterizing the adsorption activity of $\text{Fe}_{\text{SA}}@V_x\text{-N}_y$. As_2 , As_4 , AsO and AsH_3 can be stably adsorbed when the temperature is below 1100 K. In the same simulation system, four molecules will compete for adsorption sites, of which As_2 and AsO have more competitive advantages. A competitive adsorption behavior exists between As_2 and AsO at 300 to 900 K, and AsO has relatively stronger adsorption capacity. This theoretical research provides further insights into arsenic pollutant adsorption, enabling potential new processes for the synergistic removal of hazardous pollutants in exhaust gases from integrated gasification combined cycle coal plants, such as mercury, arsenic and lead.

Conflicts of interest

There are no conflicts to declare.

Acknowledgements

This work was supported by the Natural Science Foundation of Hebei Province of China (B2018502067) and the Fundamental Research Funds for the Central Universities (2020MS104).

References

- H. T. Oh, W. S. Lee, Y. Ju and C. H. Lee, Performance evaluation and carbon assessment of IGCC power plant with coal quality, *Energy*, 2019, **188**, 116063.

- 2 B. Erlach, M. Schmidt and G. Tsatsaronis, Comparison of carbon capture IGCC with pre-combustion decarbonisation and with chemical-looping combustion, *Energy*, 2011, **36**, 3804–3815.
- 3 C. G. Sotomayor, D. Groothof, J. J. Vodegel, T. A. Gacitua, A. W. Gomes-Neto, M. C. J. Oste, R. A. Pol, C. Ferreccio, S. P. Berger, G. Chong, R. H. J. A. Slart, R. Rodrigo, G. J. Navis, D. J. Touw and S. J. L. Bakker, Circulating Arsenic is Associated with Long-Term Risk of Graft Failure in Kidney Transplant Recipients: A Prospective Cohort Study, *J. Clin. Med.*, 2020, **9**, 417.
- 4 Z. Rahman and V. P. Singh, The relative impact of toxic heavy metals (THMs) (arsenic (As), cadmium (Cd), chromium (Cr)(vi), mercury (Hg), and lead (Pb)) on the total environment: an overview, *Environ. Monit. Assess.*, 2019, **191**, 1–21.
- 5 M. A. López-Antón, M. Díaz-Somoano, J. L. G. Fierro and M. R. Martínez-Tarazona, Retention of arsenic and selenium compounds present in coal combustion and gasification flue gases using activated carbons, *Fuel Process. Technol.*, 2007, **88**, 799–805.
- 6 C. Charpentreau, R. Seneviratne, A. George, M. Millan, D. R. Dugwell and R. Kandiyoti, Screening of low cost sorbents for arsenic and mercury capture in gasification systems, *Energy Fuels*, 2007, **21**, 2746–2750.
- 7 M. R. M. N.-T. M. Diaz-Somoano, Trace element evaporation during coal gasification based on a thermodynamic equilibrium calculation approach, *Fuel*, 2003, **82**, 9.
- 8 L. Otero-Gonzalez, S. V. Mikhalovsky, M. Vaclavikova, M. V. Trenikhin, A. B. Cundy and I. N. Savina, Novel nanostructured iron oxide cryogels for arsenic (As(III)) removal, *J. Hazard. Mater.*, 2020, **381**, 120996.
- 9 A. Islam, S. H. Teo, M. T. Ahmed, S. Khandaker, M. L. Ibrahim, D. N. Vo, G. Abdulkreem-Alsultan and A. S. Khan, Novel micro-structured carbon-based adsorbents for notorious arsenic removal from wastewater, *Chemosphere*, 2021, **272**, 129653.
- 10 J. P. Trembly, R. S. Gemmen and D. J. Bayless, The effect of IGFC warm gas cleanup system conditions on the gas–solid partitioning and form of trace species in coal syngas and their interactions with SOFC anodes, *J. Power Sources*, 2007, **163**, 986–996.
- 11 R. L. Hao, Z. Wang, X. Z. Mao, Y. P. Gong, B. Yuan, Y. Zhao, B. J. Tian and M. Qi, Elemental mercury removal by a novel advanced oxidation process of ultraviolet/chlorite-ammonia: Mechanism and kinetics, *J. Hazard. Mater.*, 2019, **374**, 120–128.
- 12 S. T. Liu, J. M. Chen, Y. Cao, H. K. Yang, C. M. Chen and W. B. Jia, Distribution of mercury in the combustion products from coal-fired power plants in Guizhou, southwest China, *J. Air Waste Manage.*, 2019, **69**, 234–245.
- 13 X. Q. Wang, H. Q. Huang, Q. Q. Zhou, P. Ning, J. H. Cheng, Y. L. Lin, L. L. Wang and Y. B. Xie, High-Performance Arsenic Removal Using $\text{CuO}_x/\text{TiO}_2$ Sorbents under Low-Temperature Conditions, *Energy Fuels*, 2018, **32**, 7035–7045.
- 14 C. B. Wang, Y. Zhang and H. M. Liu, Experimental and Mechanism Study of Gas-Phase Arsenic Adsorption Over $\text{Fe}_2\text{O}_3/\text{gamma-Al}_2\text{O}_3$ Sorbent in Oxy-Fuel Combustion Flue Gas, *Ind. Eng. Chem. Res.*, 2016, **55**, 10656–10663.
- 15 S. L. Zhao, D. Pudasainee, Y. F. Duan, R. Gupta, M. Liu and J. H. Lu, A review on mercury in coal combustion process: Content and occurrence forms in coal, transformation, sampling methods, emission and control technologies, *Prog. Energy Combust.*, 2019, **73**, 26–64.
- 16 X. Hu, Q. Lu, Y. Sun and J. Zhang, Mechanism of trace element adsorption on a clean and S pre-coated Pd(111) surface: insight from density functional theory calculations, *Fuel*, 2013, **107**, 290–298.
- 17 S. Poulston, E. J. Granite, H. W. Pennline, H. Hamilton and A. W. J. Smith, Palladium based sorbents for high temperature arsine removal from fuel gas, *Fuel*, 2011, **90**, 3118–3121.
- 18 J. P. Baltrus, E. J. Granite, H. W. Pennline, D. Stanko, H. Hamilton, L. Rowsell, S. Poulston, A. Smith and W. Chu, Surface characterization of palladium-alumina sorbents for high-temperature capture of mercury and arsenic from fuel gas, *Fuel*, 2010, **89**, 1323–1325.
- 19 S. J. Sun, D. S. Zhang, C. Y. Li, Y. J. Wang and Q. S. Yang, Density functional theory study of mercury adsorption and oxidation on CuO(111) surface, *Chem. Eng. J.*, 2014, **258**, 128–135.
- 20 H. T. Zhao, S. Liu, W. T. Lo, F. Enujekwu, C. H. Zheng, S. Y. Yu, X. Gao and T. Wu, Mechanism of Hg^0 and O_2 Interaction on the $\text{IrO}_2(110)$ Surface: A Density Functional Theory Study, *Energy Fuels*, 2019, **33**, 1354–1362.
- 21 S. A. Siddiqui, N. Bouarissa, T. Rasheed and M. S. Al-Assiri, Quantum chemical study of the interaction of elemental Hg with small neutral, anionic and cationic Au_n ($n = 1-6$) clusters, *Mater. Res. Bull.*, 2013, **48**, 995–1002.
- 22 L. S. Sun, A. C. Zhang, S. Su, H. Wang, J. L. Liu and J. Xiang, A DFT study of the interaction of elemental mercury with small neutral and charged silver clusters, *Chem. Phys. Lett.*, 2011, **517**, 227–233.
- 23 D. Kim, Y. Ren, M. Cui, Y. Lee, J. Kim, O. Kwon, W. Ji and J. Khim, Arsenic adsorption on two types of powdered and beaded coal mine drainage sludge adsorbent, *Chemosphere*, 2021, **272**, 129560.
- 24 W. J. Yang, X. S. Liu, X. L. Chen, Y. Cao, S. P. Cui, L. Jiao, C. C. Wu, C. M. Chen, D. Fu, I. D. Gates, Z. Y. Gao and H. L. Jiang, A sulfur-tolerant MOF-based single-atom Fe catalyst for efficient oxidation of NO and Hg^0 , *Adv. Mater.*, 2022, 2110123.
- 25 Y. Tang, Z. Liu, Z. Shen, W. Chen, D. Ma and X. Dai, Adsorption sensitivity of metal atom decorated bilayer graphene toward toxic gas molecules (CO, NO, SO_2 and HCN), *Sens. Actuators, B*, 2017, **238**, 182–195.
- 26 Z. Gao, S. Xu, L. Li, G. Yan, W. Yang, C. Wu and I. D. Gates, On the adsorption of elemental mercury on single-atom TM (TM = V, Cr, Mn, Co) decorated graphene substrates, *Appl. Surf. Sci.*, 2020, **516**, 146037.
- 27 Y. Zhang, C. Wang and H. Liu, Experiment and mechanism research on gas-phase As_2O_3 adsorption of $\text{Fe}_2\text{O}_3/\gamma\text{-Al}_2\text{O}_3$, *Fuel*, 2016, **181**, 1034–1040.
- 28 K. Q. He, C. G. Yuan, Y. H. Jiang, X. L. Duan, Y. Li and M. D. Shi, Synergistic effects of Fe–Mn binary oxide for

- gaseous arsenic removal in flue gas, *Ecotoxicol. Environ. Saf.*, 2021, **207**, 111491.
- 29 P. H. Li, M. Yang, Y. X. Li, Z. Y. Song, J. H. Liu, C. H. Lin, J. Zeng and X. J. Huang, Ultra-Sensitive and Selective Detection of Arsenic(III) via Electroanalysis over Cobalt Single-Atom Catalysts, *Anal. Chem.*, 2020, **92**, 6128–6135.
- 30 Y. Tang, W. Chen, C. Li, L. Pan, X. Dai and D. Ma, Adsorption behavior of Co anchored on graphene sheets toward NO, SO₂, NH₃, CO and HCN molecules, *Appl. Surf. Sci.*, 2015, **342**, 191–199.
- 31 Y. N. Tang, Z. Y. Liu, Z. G. Shen, W. G. Chen, D. W. Ma and X. Q. Dai, Adsorption sensitivity of metal atom decorated bilayer graphene toward toxic gas molecules (CO, NO, SO₂ and HCN), *Sens. Actuators, B*, 2017, **238**, 182–195.
- 32 W. Yang, Z. Gao, X. Ding, G. Lv and W. Yan, The adsorption characteristics of mercury species on single atom iron catalysts with different graphene-based substrates, *Appl. Surf. Sci.*, 2018, **455**, 940–951.
- 33 W. Yang, Z. Gao, X. Liu, X. Ding and W. Yan, The adsorption characteristics of As₂O₃, Pb⁰, PbO and PbCl₂ on single atom iron adsorbent with graphene-based substrates, *Chem. Eng. J.*, 2019, **361**, 304–313.
- 34 Y. L. Liu, H. Li, W. L. Cen, J. J. Li, Z. M. Wang and G. Henkelman, A computational study of supported Cu-based bimetallic nanoclusters for CO oxidation, *Phys. Chem. Chem. Phys.*, 2018, **20**, 7508–7513.
- 35 H. Li, S. Guo, K. Shin, M. S. Wong and G. Henkelman, Design of a Pd–Au Nitrite Reduction Catalyst by Identifying and Optimizing Active Ensembles, *ACS Catal.*, 2019, **9**, 7957–7966.
- 36 E. J. Evans, H. Li, S. Han, G. Henkelman and C. B. Mullins, Oxidative Cross-Esterification and Related Pathways of Co-Adsorbed Oxygen and Ethanol on Pd–Au, *ACS Catal.*, 2019, **9**, 4516–4525.
- 37 W. Yang, J. Ren, H. Zhang, J. Li, C. Wu, I. Gates and Z. Gao, Single-atom iron as a promising low-temperature catalyst for selective catalytic reduction of NO_x with NH₃: A theoretical prediction, *Fuel*, 2021, **302**, 121041.
- 38 M. Manadé, F. Viñes and F. Illas, Transition metal adatoms on graphene: A systematic density functional study, *Carbon*, 2015, **95**, 525–534.
- 39 P. Jathon, S. M. Kozlov, F. Vines, J. Limtrakul and F. Illas, Establishing the Accuracy of Broadly Used Density Functionals in Describing Bulk Properties of Transition Metals, *J. Chem. Theory Comput.*, 2013, **9**, 1631–1640.
- 40 H. Yang, Y. Liu, Y. Luo, S. Lu, B. Su and J. Ma, Achieving High Activity and Selectivity of Nitrogen Reduction via Fe–N₃ Coordination on Iron Single-Atom Electrocatalysts at Ambient Conditions, *ACS Sustainable Chem. Eng.*, 2020, **8**, 12809–12816.
- 41 A. W. Robertson, B. Montanari, K. He, J. Kim, C. S. Allen, Y. A. Wu, J. Olivier, J. Neethling, N. Harrison, A. I. Kirkland and J. H. Warner, Dynamics of single Fe atoms in graphene vacancies, *Nano Lett.*, 2013, **13**, 1468–1475.
- 42 J. Yan, J. Xia, Q. Zhang, B. Zhang and B. Wang, First-Principles Studies on the Structural and Electronic Properties of As Clusters, *Materials*, 2018, **11**, 1596.
- 43 M. Seidl, G. Balazs and M. Scheer, The Chemistry of Yellow Arsenic, *Chem. Rev.*, 2019, **119**, 8406–8434.
- 44 D. R. U. A. J. Wilcox, A Theoretical Study of Properties and Reactions Involving Arsenic and Selenium Compounds Present in Coal Combustion Flue Gases, *J. Phys. Chem. A*, 2006, **110**, 6.
- 45 Y. Li, K. Li, X. Sun, X. Song, H. Sun and P. Ning, DFT calculation of AsH₃ adsorption and dissociation on Ni- and Cu-doped graphene, *J. Mol. Model.*, 2019, **25**, 358.
- 46 J. K. Norskov, F. Abild-Pedersen, F. Studt and T. Bligaard, Density functional theory in surface chemistry and catalysis, *Proc. Natl. Acad. Sci. U. S. A.*, 2011, **108**, 937–943.
- 47 J. K. Norskov, T. Bligaard, J. Rossmeisl and C. H. Christensen, Towards the computational design of solid catalysts, *Nat. Chem.*, 2009, **1**, 37–46.
- 48 W. Zhang, J. Q. Zhu, D. J. Cheng and X. C. Zeng, PtCoNi Alloy Nanoclusters for Synergistic Catalytic Oxygen Reduction Reaction, *ACS Appl. Nano Mater.*, 2020, **3**, 2536–2544.
- 49 L. Farsi and N. A. Deskins, First principles analysis of surface dependent segregation in bimetallic alloys, *Phys. Chem. Chem. Phys.*, 2019, **21**, 23626–23637.
- 50 B. Schweitzer, C. Archuleta, B. Seong, R. Anderson and D. A. Gomez-Gualdrón, Electronic effects due to organic linker-metal surface interactions: implications on screening of MOF-encapsulated catalysts, *Phys. Chem. Chem. Phys.*, 2020, **22**, 2475–2487.
- 51 X. Mao, C. Tang, T. W. He, D. Wijethunge, C. Yan, Z. H. Zhu and A. J. Du, Computational screening of MN₄ (M = Ti–Cu) based metal organic frameworks for CO₂ reduction using the d-band centre as a descriptor, *Nanoscale*, 2020, **12**, 6188–6194.
- 52 B. Huang, L. Xiao, J. T. Lu and L. Zhuang, Spatially Resolved Quantification of the Surface Reactivity of Solid Catalysts, *Angew. Chem., Int. Ed.*, 2016, **55**, 6239–6243.
- 53 Y. Zhang, X. S. Chen, Y. Huang, C. Zhang, F. Li and H. B. Shu, The Role of Intrinsic Defects in Electrocatalytic Activity of Monolayer VS₂ Basal Planes for the Hydrogen Evolution Reaction, *J. Phys. Chem. C*, 2017, **121**, 1530–1536.